

## Observations of Microstructure-Oriented Crack Growth in a Cast Mg-Al-Ba-Ca Alloy under Tension, Compression and Fatigue

Maier, Petra; Ginesta, Daniel; Clausius, Benjamin; Hort, Norbert

*Published in:*  
Metals

*DOI:*  
[10.3390/met12040613](https://doi.org/10.3390/met12040613)

*Publication date:*  
2022

*Document Version*  
Publisher's PDF, also known as Version of record

[Link to publication](#)

*Citation for published version (APA):*  
Maier, P., Ginesta, D., Clausius, B., & Hort, N. (2022). Observations of Microstructure-Oriented Crack Growth in a Cast Mg-Al-Ba-Ca Alloy under Tension, Compression and Fatigue. *Metals*, 12(4), Article 613.  
<https://doi.org/10.3390/met12040613>

### General rights

Copyright and moral rights for the publications made accessible in the public portal are retained by the authors and/or other copyright owners and it is a condition of accessing publications that users recognise and abide by the legal requirements associated with these rights.



- Users may download and print one copy of any publication from the public portal for the purpose of private study or research.
- You may not further distribute the material or use it for any profit-making activity or commercial gain
- You may freely distribute the URL identifying the publication in the public portal ?

### Take down policy

If you believe that this document breaches copyright please contact us providing details, and we will remove access to the work immediately and investigate your claim.

## Article

# Observations of Microstructure-Oriented Crack Growth in a Cast Mg-Al-Ba-Ca Alloy under Tension, Compression and Fatigue

Petra Maier <sup>1,\*</sup> , Daniel Ginesta <sup>1</sup>, Benjamin Clausius <sup>1</sup> and Norbert Hort <sup>2,3</sup> 

<sup>1</sup> School of Mechanical Engineering, University of Applied Sciences Stralsund, 18435 Stralsund, Germany; daniel.m.roque@hochschule-stralsund.de (D.G.); benjamin.clausius@hochschule-stralsund.de (B.C.)

<sup>2</sup> Functional Materials, Helmholtz-Zentrum Hereon, 21502 Geesthacht, Germany; norbert.hort@hereon.de

<sup>3</sup> Institute of Product and Process Innovation, Leuphana University Lüneburg, 21335 Lüneburg, Germany

\* Correspondence: petra.maier@hochschule-stralsund.de

**Abstract:** DieMag633, a cast Mg-Al-Ba-Ca alloy, was the focus of this study. Brittle interdendritic phases strongly influenced the crack initiation and propagation under quasi-static and fatigue loading. Especially under tensile loading, the material showed a low resistance to failure. Selected fatigue loading sequences were applied to investigate their influence on crack propagation. DieMag633 in this study contained shrinkage cavities and pores of significant size and irregular distribution. Even though pores played a role in initiating the crack, it was mainly influenced by the Ba- and Ca-rich phases, being and staying much harder under deformation than the Mg-matrix. Apart from the fatigue crack propagation region under fatigue loading, there was no transgranular cracking found within the dendritic  $\alpha$ -Mg grains. Only under compression did the dendritic  $\alpha$ -Mg grains bridge the crack from one brittle phase to another. Transgranular cracking within the compact Ba-rich phase was very pronounced, starting with many microcracks within this phase and then connecting to the macrocrack. The lamellar Ca-rich phase showed also mainly transgranular cracking, but being small lamellae, intergranular cracking was additionally found. The hardness increase under deformation depended on the loading condition; a compression load strain-hardened the material the most.  $\mu$ CT analysis was applied to characterize the amount and location of the shrinkage cavities and pores in the individual gauge length.

**Keywords:** microstructure; crack propagation; brittle phases; porosity; fatigue;  $\mu$ -CT analysis



**Citation:** Maier, P.; Ginesta, D.; Clausius, B.; Hort, N. Observations of Microstructure-Oriented Crack Growth in a Cast Mg-Al-Ba-Ca Alloy under Tension, Compression and Fatigue. *Metals* **2022**, *12*, 613. <https://doi.org/10.3390/met12040613>

Academic Editors: Menachem Bamberger and Daolun Chen

Received: 26 February 2022

Accepted: 31 March 2022

Published: 2 April 2022

**Publisher's Note:** MDPI stays neutral with regard to jurisdictional claims in published maps and institutional affiliations.



**Copyright:** © 2022 by the authors. Licensee MDPI, Basel, Switzerland. This article is an open access article distributed under the terms and conditions of the Creative Commons Attribution (CC BY) license (<https://creativecommons.org/licenses/by/4.0/>).

## 1. Introduction

The die-cast Mg-Al-Ba-Ca alloy, called DieMag633, was developed as a creep resistant alloy based on Mg-Al. Rare earths elements (REE) are often chosen as alloying elements when a good creep resistance is desired in Mg-Al alloys. This is based on the formation of precipitates like  $Al_{11}RE_3$ ,  $Al_4RE$  and  $Al_2RE$  [1,2]. Alloying with Ba and Ca replaces the expensive and limited REE, strengthening precipitates where expected. Based on AXJ520 [3] and AX52/AX53 [4], where  $(Mg,Al)_2Ca$  precipitates strengthen the alloys, and based on Mg-Zn alloys, where alloying with Ba promotes both the formation of strengthening precipitates by stimulating the precipitate nucleation and the acceleration of the kinetics of precipitation during artificial and natural ageing [5], a Mg-Al-Ba-Ca alloy was developed as a creep resistant alloy [6,7].

In this study the DieMag633 alloy, according to their alloying elements also known as ABaX633, consists mainly of primary dendrites of  $\alpha$ -Mg and two interdendritic phases of different morphology. Increasing the amount of Al, Ca and Ba in the DieMag-series (DieMag211, DieMag422 and DieMag633—numbers stand for amount of Al, Ca and Ba in wt.%) increases strength and creep resistance based on the increasing amount of  $Al_2Ca$  and  $Mg_{21}Al_3Ba_2$  [7]. In the study by Dieringa et al. [6] it can be seen that the DieMag422

shows higher threshold stresses than AE42 and MRI230D, which results in an excellent creep resistance. EDXS point measurements in [8] show little to no Ba-content in the lamellar  $\text{Al}_2\text{Ca}$  phase and a significant concentration of Ba in the  $\text{Mg}_{21}\text{Al}_3\text{Ba}_2$  phase. The as-cast DieMag633 in study [8] had a porosity of 1.48%, a tensile yield strength (TYS) of  $202.6 \pm 0.7$  MPa, an ultimate tensile strength (UTS) of  $229.6 \pm 5.8$  MPa, an elongation at fracture (El.) of  $1.6 \pm 0.5\%$ , and a compression yield strength (CYS) of  $117.6 \pm 15.1$  MPa. The DieMag633 in study [8] showed the best creep resistance at higher stresses of 90 and 100 MPa among the alloys investigated: AE42, AE44, MRI230D, DieMag211, DieMag422 and DieMag633.

DieMag422 was investigated with the mechanical properties of TYS, here 0.01, at 15 MPa, UTS at 122 MPa and El at 1.72% [9–11]. Scanning electron microscope (SEM) images and EDX studies showed that the grain boundaries of the primary  $\alpha$ -Mg phase separate the compact Ba-rich phase with an area fraction of approximately 5.0%, and the lamellar Ca-rich phase of an area fraction of approximately of 10.8%. Potentiodynamic polarization measurements studies showed a selective corrosive attack between the  $\alpha$ -Mg phase and the lamellar Ca-rich phase. The estimated endurance limit was found to be 45 MPa at 10 Hz at a load ratio of  $R = -1$  and a failure stress amplitude 72 MPa, respectively in [9,10], and to be 64 MPa for the estimated fatigue limit and 99 MPa for the failure stress amplitude in [11]. The DieMag422 shows strong concentration-dependent corrosion resistance in chloride-containing electrolytes. The alloy exhibits a poor corrosion resistance but a homogeneous material corrosion and therefore, a linear relation between fatigue strength and corrosion rate [12].

The cast DieMag442 in the study by Teschke et al. [13], where the fatigue behavior was of interest in comparison to AE42, showed large irregularly distributed pores. Most of the pores had a diameter between 25 and 175  $\mu\text{m}$  and a few pores were even larger than 290  $\mu\text{m}$ . The following mechanical properties were presented in that study: TYS at  $78.1 \pm 0.6$  MPa, UTS at  $114.6 \pm 3.5$  MPa, CYS at  $128.0 \pm 4.9$  MPa and ultimate compression strength (UCS) at  $286.8 \pm 2.9$  MPa. These properties resulted in a tension–compression yield asymmetry of 0.61—opposite in character to many other studies [14–16] and to the investigated AE42 in the study by Teschke et al. [13] with a value of 1.51. In a study by Park et al. [16] the yield-asymmetry below 1 in a cast AZ31 alloy was explained by the high value of the Schmid factors in the {1012} twin formation in the tensile direction. However, in study [13] the compression–compression fatigue strength of DieMag422 at increased temperature was higher than that of AE42. The results of the quasi-static compression and compression–compression fatigue tests show a  $\sim 45^\circ$  fracture with respect to the compression test axis, which respects the direction of maximum shear stress. The fracture was found to grow intercrystalline (intergranular/interdendritic) in the middle of the specimen, whereas in the edge areas, the crack grew transcrystalline (transgranular within the dendritic Mg-matrix). Parallel to the main crack, further small transcrystalline sub-cracks were observed at an angle of  $45^\circ$ . A correlation with the accumulation of pores of various sizes was expected. Fatigue cracks initiating from porosity were also seen in the study in [17] on AZ91D-T6 alloy samples. A dependence of the crack propagation on the fracture mode was found in [18]; here transdendritic cracking occurred under fatigue and interdendritic cracking in overload.

The influence of interdendritic precipitations on fracture behavior was studied in various alloys: in Al-Zn-Mg-Cu alloys, where the network structure of grain boundary precipitates  $\text{S-(Al}_2\text{CuMg)}$  and  $\text{Al}_7\text{Cu}_2\text{Fe}$  link together to create the crack propagation [19]; in A356.2, where Si particles or  $\beta\text{-Al}_5\text{FeSi}$  platelets split due to their brittleness and guide the crack or the crack propagates through the well-modified Si eutectic regions [20], which was also seen in [21] for the low-pressure die cast A356 alloy.

In the study by Zyka et al. [22] on mechanical properties and microstructure of large IN713LC nickel superalloy castings, several non-connected cracks were seen at interdendritic carbides as sub-cracks near the main fracture surface. The orientation of the interdendritic carbides influences the elongation at fracture: in specimens with low elon-

gation, carbide platelets are oriented perpendicular to the tensile stress, thus promoting their longitudinal cracking and interconnecting of such cracks while in specimens with high tensile elongation, the angle between carbide platelets and tensile direction is smaller.

The cast 20Cr32Ni + Nb alloy investigated in [23] consisted of brittle NbC carbide particles, which showed cracks at the macroscopic scale, well below the final failed interdendritic fracture surface. However, the fracture surface was also characterized by dimples at the microscale, so cracking via micro-void nucleation and coalescence, intermixed with cleavage in the carbide particles was concluded. Due to the austenitic matrix being tough enough to stop initial cracks generated in the carbide particles, this study showed, that NbC cracking cannot be the determinant factor for final sample fracture. However, the nucleated carbide microfracture still triggers ductile fracture along the austenite grain boundary, which leads to final fracture.

Obviously, the crack growth is guided by hard and brittle interdendritic second phases, which fail much earlier than the softer matrix because of lack of deformation ability. In the DieMag-series, the second phases are also found to be harder than the dendritic Mg-matrix. In [6] the DieMag422 had a Vickers hardness of  $51 \pm 2$  HV<sub>10</sub>, where the individual phases showed HV<sub>0.005</sub> of  $166 \pm 24$  HV for Mg<sub>21</sub>Al<sub>3</sub>Ba<sub>2</sub>,  $95 \pm 9$  HV for Al<sub>2</sub>Ca and  $59 \pm 11$  HV for the  $\alpha$ -Mg matrix. The total phase fraction from the Mg<sub>21</sub>Al<sub>3</sub>Ba<sub>2</sub> and Al<sub>2</sub>Ca phases was ~9.5% and 6.6%, respectively. In [9] the DieMag422 had a Vickers hardness of  $53 \pm 2.0$  HV<sub>10</sub>, where the individual phases showed HV<sub>0.005</sub> of 222 HV for Mg<sub>21</sub>Al<sub>3</sub>Ba<sub>2</sub>, 116 HV for Al<sub>2</sub>Ca and 67 HV for the  $\alpha$ -Mg matrix at the edge of the sample, and in the sample middle: 353 HV for Mg<sub>21</sub>Al<sub>3</sub>Ba<sub>2</sub>, 78 HV for Al<sub>2</sub>Ca and 67 HV for the  $\alpha$ -Mg matrix.

Based on previous studies, especially in [13] and the literature review, to determine more detail of the microstructure-oriented crack growth was of interest. The role of the phases in deformation and crack propagation under different load conditions will help the understanding of fracture mechanics in Mg-Al-Ba-Ca alloys and will provide information about preferred load conditions or limited load conditions, and thus the selected application sites. It was also thought to be of interest of how pores and shrinkage cavities influence mechanical properties and fracture location.

## 2. Materials and Methods

The DieMag633 used in this study was produced by high-pressure die casting (HPDC) according to [6]. The melt bath temperature was 720 °C. The alloy was cast in preheated cylindrical mold of 300 °C and a diameter of 130 mm and a length of 250 mm. The samples were first cut in rectangular sizes and then machined with a CNC turning machine to the final specimen shape, including surface finishing. For microstructural investigations specimens were ground and polished. Etching with picric acid was not needed to study the interaction of crack propagation with the phases in the microstructure. When applying the etching procedure using picric acid for only a few seconds, twins in the microstructure became visible. Optical microscopy was carried out with an LEICA DMi8 A microscope (Leica Microsystems GmbH, Wetzlar, Germany).

The  $\mu$ -CT measurements were performed with a Bruker Skyscan 2214 (Bruker, Billerica, MA, USA). For scanning electron microscopy, a TESCAN VEGA4 (TESCAN ORSAY HOLDING, Brno, Czech Republic) was used. For mechanical testing the servo-hydraulic test system MTS 250 (MTS Systems, Eden Prairie, MN, USA) was used and Vickers hardness HV<sub>0.005</sub> (indentation load of 0.049 N) was measured with a Zeiss Neophot 2 (Carl Zeiss Jena GmbH, Jena, Germany) with at least 10 indents per phase investigated. Microhardness measurements were performed in the vicinity of the fracture surfaces. Samples for tensile and fatigue loading had a gauge length of 30 mm and a lowest diameter of 5 mm. The radius for the transition to the smaller gauge length from the clamping part of 10 mm was 46 mm, and the overall length of the samples was 90 mm. The cylindrical samples for compression had a diameter of 10 mm and a height of 15 mm. For tensile and compression tests, five samples were used, and for the fatigue tests two samples were used. All mechanical



testing was performed at room temperature. For unidirectional testing ( $R = 0$  and  $R = -\infty$ ), where  $R$  is the stress ratio) a stress of 50 MPa and  $-50$  MPa was applied, and the same stress level was applied for the fully reversed testing ( $R = -1$ ). The cyclic stress–strain data were monitored to calculate the associated hysteresis loops, which allow statements on cyclic creep (progressive change of mean strain by tensile or compressive deformation under repeated load cycles).

To date, only a few samples have been tested; for statistical data on cycles at fracture, further tests are in progress. The focus in this study was on the interaction of crack propagation with microstructure, rather than on the mechanical properties.

### 3. Results

The DieMag633 alloy in this study consisted of 6.54 wt.% Al, 2.71 wt.% Ba and 2.76 wt.% Ca and showed a coarse dendritic microstructure. The micrograph in Figure 1a shows the microstructure consisting of primary dendrites of  $\alpha$ -Mg and the two interdendritic and intergranular phases  $\text{Al}_2\text{Ca}$  and  $\text{Mg}_{21}\text{Al}_3\text{Ba}_2$ .  $\text{Al}_2\text{Ca}$  is the lamellar Ca-rich phase (eutectic part of the microstructure), where lamellae have a thickness of 1–3  $\mu\text{m}$  and  $\text{Mg}_{21}\text{Al}_3\text{Ba}_2$  is the Ba-rich blocky compact phase, both forming an almost closed network along the dendritic arm spacings [6]. The alloy in this study had inhomogeneously distributed shrinkage cavities of significant amount and sizes in the mm-range, see Figure 1b.

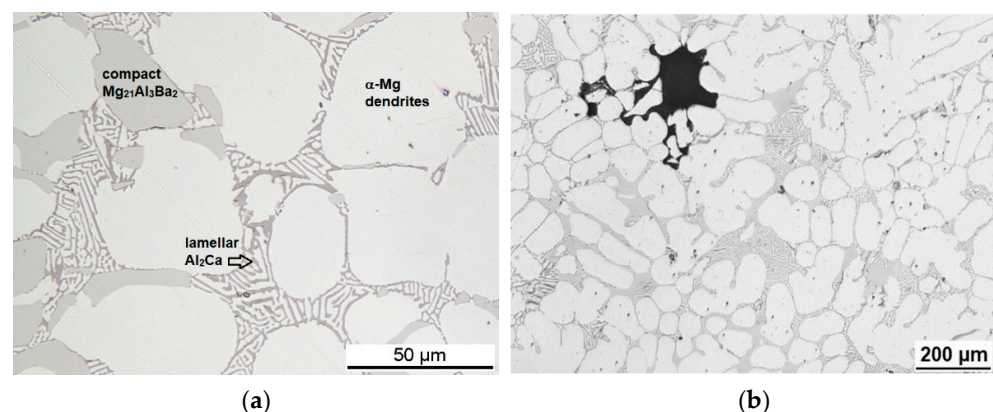


**Figure 1.** Micrographs of DieMag633 presenting interdendritic network of second phases  $\text{Mg}_{21}\text{Al}_3\text{Ba}_2$  and  $\text{Al}_2\text{Ca}$  (a) and porosity and shrinkage cavities in black color (b).

The representative  $\mu$ -CT images in Figure 2a–c show the gauge length of the sample before loading. Figure 2a,b present the homogeneous distribution of the second phases, which are made visible by filtering in Figure 2b. The pores and shrinkage cavities are highlighted in darker grey in Figure 2c. There are shrinkage cavities, which reach the mm-range—in the case of the gauge length in Figure 2c, in the upper part near the transition to the larger diameter. Due to the significant amount and size of the large shrinkage cavities, low mechanical properties under tensile load are found as well as a high scattering under fatigue load. Other than that seen in [8], but in more agreement with [9–13], the TYS was  $51.57 \pm 2.36$  MPa, the UTS  $102.11 \pm 3.48$  MPa and the El. only  $0.58 \pm 0.05\%$ . The fracture surface was not always located at the region of the lowest diameter in the gauge length—most likely influenced by larger shrinkage cavities which could sometimes be seen on the surface of the gauge length. Under compression, the CYS was  $135.00 \pm 9.17$  MPa, the UCS  $282.55 \pm 4.42$  MPa and the deformation at fracture  $11.18 \pm 0.60\%$ . The following samples according to their cycles at fracture were used for characterization in this study: fully reversed testing at 50 MPa ( $R = -1$ ) with 12,000 cycles at fracture; fully reversed testing at 50 MPa ( $R = -1$ ) with  $2 \times 10^6$  cycles run out followed by a tensile test; unidirectional testing at 50 MPa ( $R = 0$ ) with 43,300 cycles at fracture; unidirectional testing at  $-50$  MPa ( $R = -\infty$ ) with  $2 \times 10^6$  cycles run out followed by a tensile test.

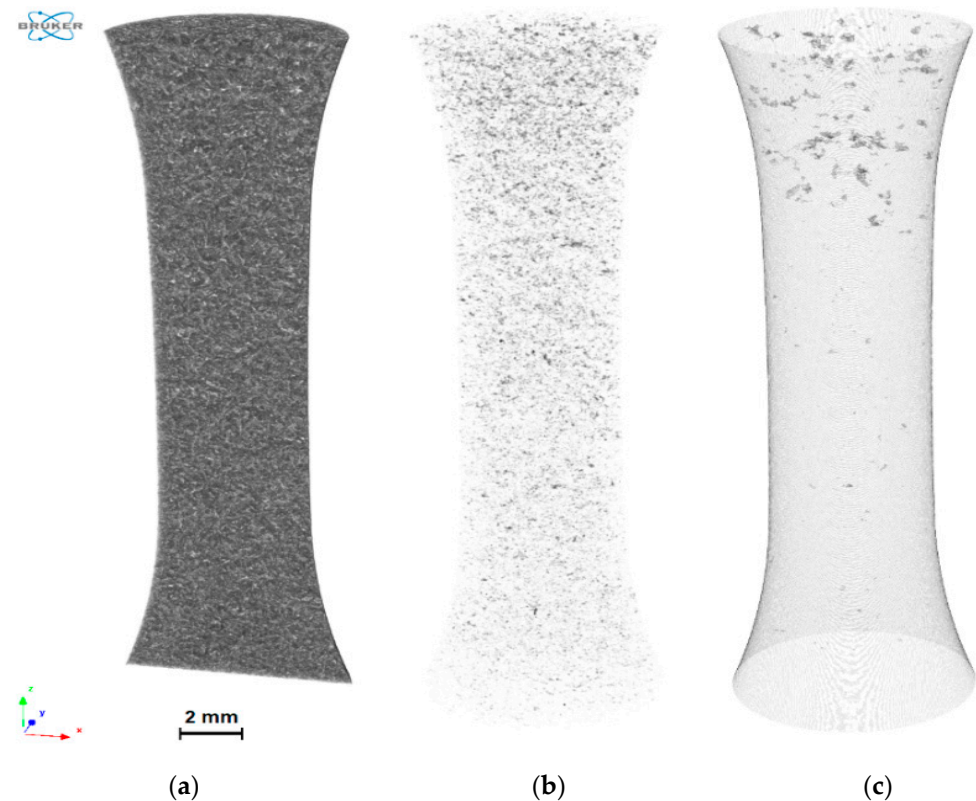


**Figure 2.** The  $\mu$ -CT images of microstructure (a), second phases (b) and pores and shrinkage cavities (c) in the gauge length of a sample before loading.

Table 1 shows that the compact Ba-rich phase  $\text{Mg}_{21}\text{Al}_3\text{Ba}_2$  shows the highest initial hardness and the dendritic Mg-matrix the lowest value. The hardness of the lamellar  $\text{Al}_2\text{Ca}$  is obviously influenced by the Mg-matrix in between the thin  $\text{Al}_2\text{Ca}$  lamellae (eutectic part of the microstructure). It can be seen that the phases do not change significantly in hardness under tensile and fatigue loading ( $R = 0$ ), but rather under compression and fatigue ( $R = -1$ ). The Mg-matrix strain-hardens the most under compression, followed by fatigue ( $R = -1$ ). The hardness increase of the Ba-rich phase  $\text{Mg}_{21}\text{Al}_3\text{Ba}_2$  Mg-matrix is less pronounced than that of the lamellar Ca-rich phase  $\text{Al}_2\text{Ca}$ .

**Table 1.** Hardness (HV0.005, average values) of  $\alpha$ -Mg,  $\text{Al}_2\text{Ca}$  and  $\text{Mg}_{21}\text{Al}_3\text{Ba}_2$  of the initial microstructure before and after the different loading conditions.

	$\alpha$ -Mg	$\text{Al}_2\text{Ca}$	$\text{Mg}_{21}\text{Al}_3\text{Ba}_2$
Initial	$58.5 \pm 6.9$	$139.9 \pm 14.5$	$249.9 \pm 42.8$
Tensile	$64.8 \pm 12.3$	$146.5 \pm 25.3$	$275.6 \pm 46.6$
Compression	$89.5 \pm 10.8$	$193.3 \pm 28.5$	$320.7 \pm 42.6$
Fatigue, $R = -1$	$78.7 \pm 11.3$	$180.3 \pm 24.9$	$308.6 \pm 47.2$
Fatigue, $R = 0$	$62.4 \pm 3.9$	$146.3 \pm 17.4$	$275.1 \pm 37.4$

Figure 3 shows representative cross-sectional micrographs of the fracture surfaces after tensile load (Figure 3a), compression load (Figure 3b) and fatigue load (Figure 3c). The main crack and the sub-cracks follow the networked blocky and lamellar second phases. The images in Figures 4 and 5 show the crack propagation of the sub-cracks near the main crack and its interaction with the microstructural features in more detail for tensile and compressive loading. Under tension, the crack initiates and propagates mainly through the compact Ba-rich phase  $\text{Mg}_{21}\text{Al}_3\text{Ba}_2$  due to its high hardness and brittleness (transgranular cracking). The lamellar Ca-rich phase  $\text{Al}_2\text{Ca}$  bridges the crack also mainly transgranular



into the next compact Ba-rich phase  $Mg_{21}Al_3Ba_2$ , see Figures 3a and 4a–c. Only very small lamellae of  $Al_2Ca$  show intergranular cracking along their interface to the  $\alpha$ -Mg matrix.

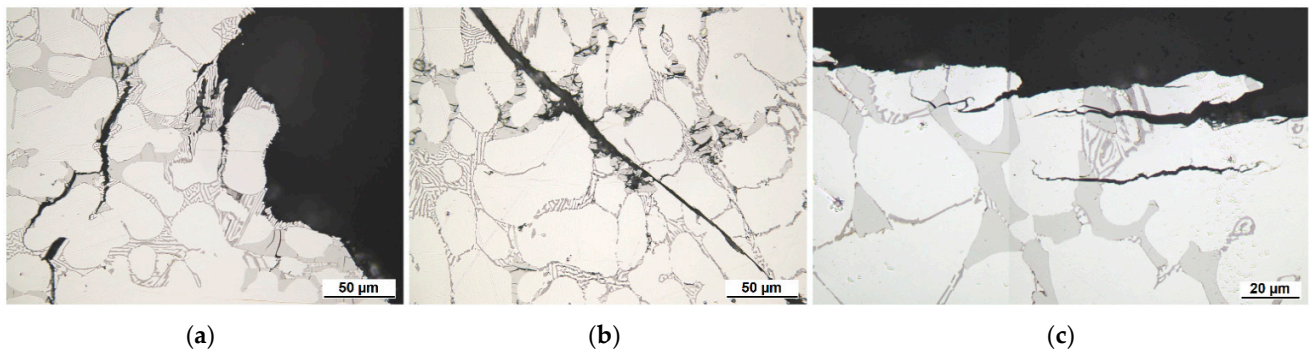


**Figure 3.** Cross-sectional micrographs of fracture surfaces after tensile load (a), compression load (b) and fatigue load (c) showing the crack propagation of the sub-cracks near the main crack and its interaction with the microstructural features.

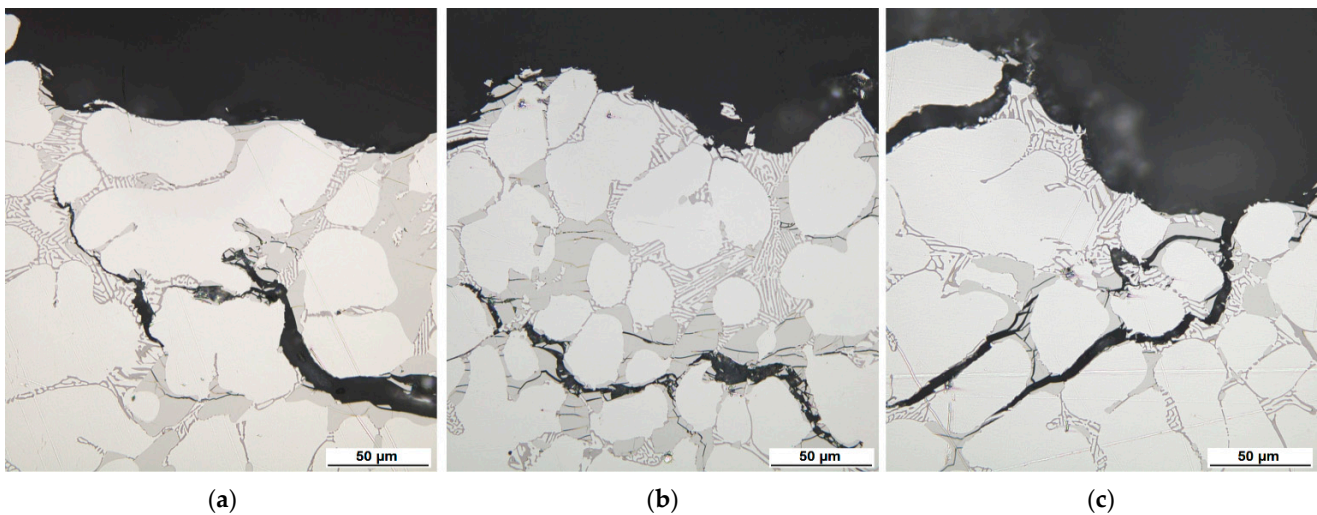


**Figure 4.** Cross-sectional micrographs of fracture surface after tensile load showing the crack propagation of the sub-cracks near the main crack and its interaction with the microstructural features (a–c).

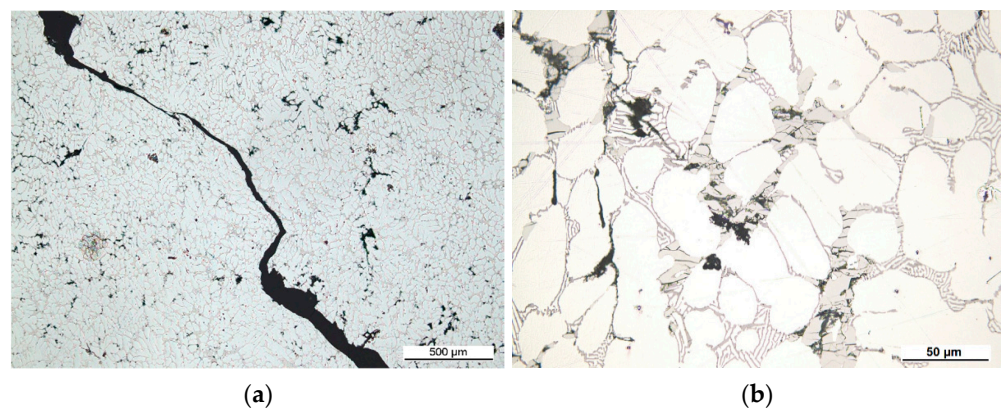


**Figure 5.** Cross-sectional micrographs of fracture surface after compression load showing the crack propagation of the sub-cracks near the main crack and its interaction with the microstructural features (a,b).

Under compression, see Figures 3b and 5a,b, the Mg-matrix also bridges the crack between the compact Ba-rich phases of  $\text{Mg}_{21}\text{Al}_3\text{Ba}_2$ , mainly supported by the Ca-rich  $\text{Al}_2\text{Ca}$  lamellae due to final high shear stress. Compression samples show a rather large plastic deformation zone: the compact Ba-rich phases of  $\text{Mg}_{21}\text{Al}_3\text{Ba}_2$  near the main crack up to the surface of the sample, show transgranular fractures, see microcracks in the compact in Figures 3b and 5b, reach even into several narrow dendritic arm spacings. The hardness increase of the compact Ba-rich phases of  $\text{Mg}_{21}\text{Al}_3\text{Ba}_2$ —up to 128% with the highest initial and strain-hardened value—is significant under compression, see Table 1.

Figure 6a–e show that under fatigue loading with a load ratio  $R = 0$  (sample reached 43,300 cycles at fracture) mainly transgranular cracking within the brittle second phases  $\text{Mg}_{21}\text{Al}_3\text{Ba}_2$  and  $\text{Al}_2\text{Ca}$  can be found. However, there is also transgranular cracking within the dendritic  $\alpha$ -Mg grains, see Figure 6c,d. The cross-sectional micrograph of the fractured surface in Figure 6e cuts the sample half-way along the crack propagation (crack initiation on the right and residual fractured surface on the left). It can be seen that the transgranular cracks within the dendritic  $\alpha$ -Mg grains are only present along the fatigue crack propagation region within the first 25% of the fractured surface. Monitoring the hysteresis revealed strain hardening during tensile creep with ongoing fatigue.

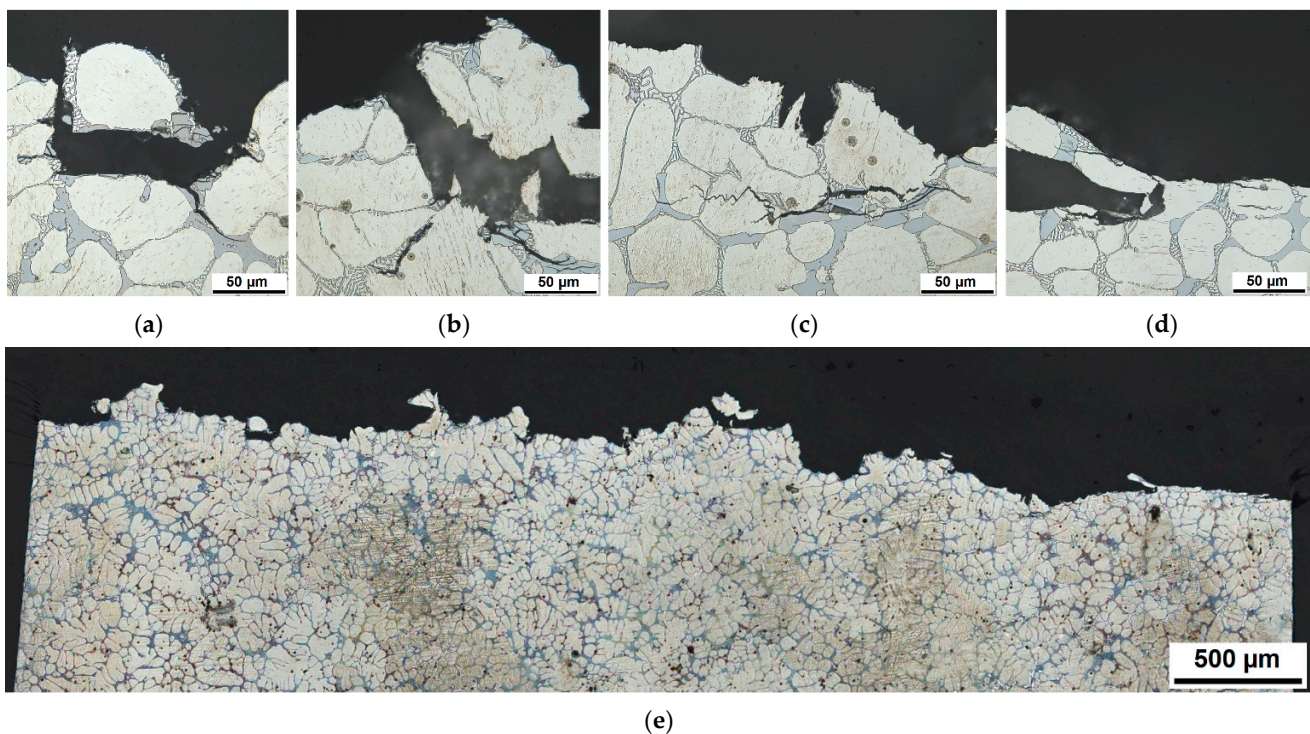


**Figure 6.** Cross-sectional micrographs of fracture surface after fatigue load ( $R = 0$ , 43,000 cycles) showing the crack propagation of the sub-cracks near the main crack and its interaction with the microstructural features (a–e).

In addition to the cross-sectional micrographs in Figure 6, Figure 7 shows the results of the  $\mu$ -CT analysis of a fracture surface after fatigue loading at a ratio  $R = 0$ . The top view in Figure 7a images the fractured sample in the direction of the crack propagation, starting from the crack initiation to the residual fracture surface. Sub-cracks become very visible. The cut to size fracture surface in Figure 7b shows the sub-cracks propagating inside the sample, even of more depth and in connection to the shrinkage cavities in the cut to the smaller size fractured surface in Figure 7c—see here the white arrows marking a sub-crack connected with a shrinkage cavity below the fracture surface. By using a cross-sectional micrograph, Figure 7d presents the depth of the sub-cracks and their connection to several



cavities, which are located near the fractured surface. The network of the second phases is seen in Figure 7e with the pores and shrinkage cavities in Figure 7f, respectively.

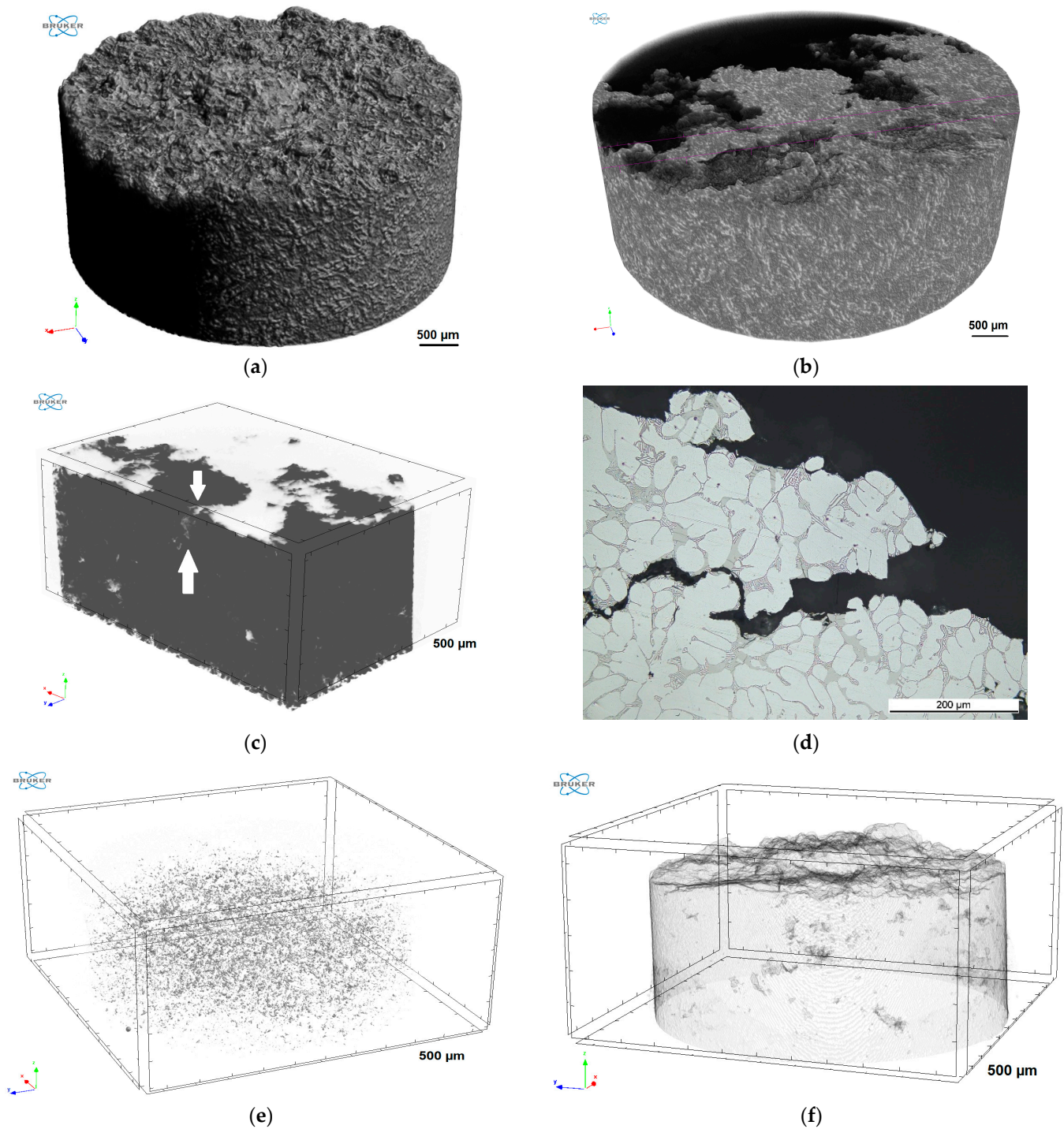


**Figure 7.** μ-CT analysis of a fracture surface after fatigue loading ( $R = 0$ , 43,300 cycles): top view in direction of crack propagation (a), cut to size fracture surface to present sub-cracks (b), cut to cross-section of fracture surface to present the depth of the sub-cracks and the connection to the shrinkage cavities (c), cross-sectional micrograph to present the depth of the sub-cracks—connected to some cavities (d), network of second phases (e) and pores and shrinkage cavities (f).

Figure 8a–e show cross-sectional micrographs of the fracture surface after fully reversed fatigue loading ( $R = -1$ ); the sample reached 12,000 cycles to fracture. The micro-



graph in Figure 8e cuts the sample halfway along the crack propagation-crack initiation on the right and the residual fractured surface on the left. Similar to the fatigue loading with a load ratio  $R = 0$ , the crack mainly follows the brittle second phases of  $Mg_{21}Al_3Ba_2$  and  $Al_2Ca$ . Only near the fatigue crack propagation region, Figure 6d, can transgranular cracking within the dendritic  $\alpha$ -Mg grains be seen. At this sample, a sub-crack below the main crack starts off in the  $\alpha$ -Mg grain. The crack is guided by the deformation twins, crossing via  $Al_2Ca$  lamellae into the adjacent  $\alpha$ -Mg grains. Transgranular cracking within the dendritic  $\alpha$ -Mg grains disappears after the fatigue crack propagation region has been passed. The fatigue hysteresis reveals strain hardening and compression creep with ongoing fatigue.

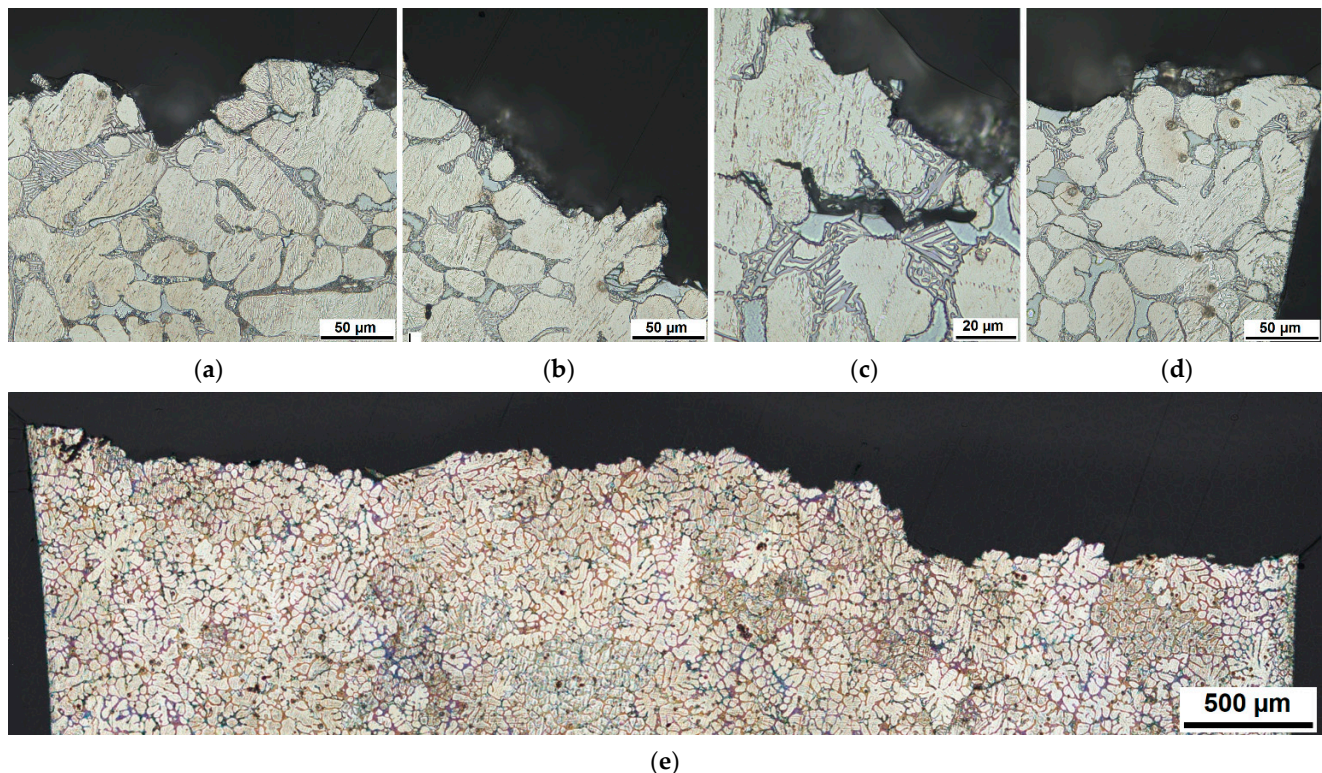


**Figure 8.** Cross-sectional micrographs of fracture surface after fatigue load ( $R = -1$ , 12,000 cycles) showing the crack propagation of the sub-cracks near the main crack and its interaction with the microstructural features (a–e).

The gauge length of a sample before loading reveals several large shrinkage cavities by  $\mu$ -CT analysis (Figure 9a,b)—two of them are located near the middle of the gauge length, where the diameter is the smallest. It is of interest whether these cavities locate the failure position. The SEM image and the reconstructed pores by the  $\mu$ -CT analysis in Figure 9c–e highlight the large shrinkage cavities in the fracture surface after the sample failed by tensile loading. During fatigue testing, the monitoring of the hysteresis loops revealed strain-hardening and showed compression creep. The following parameters were measured by the tensile test (after  $2 \times 10^6$  cycles as a “run out” at  $R = -1$ ): TYS of 97.4 MPa, UTS of 130.6 MPa, and an elongation at fracture 0.43%. The hardness increase was found mostly in the dendritic Mg-matrix of up to 124% (especially near the pore due to stress accumulation), both second phases increase up to 112%.

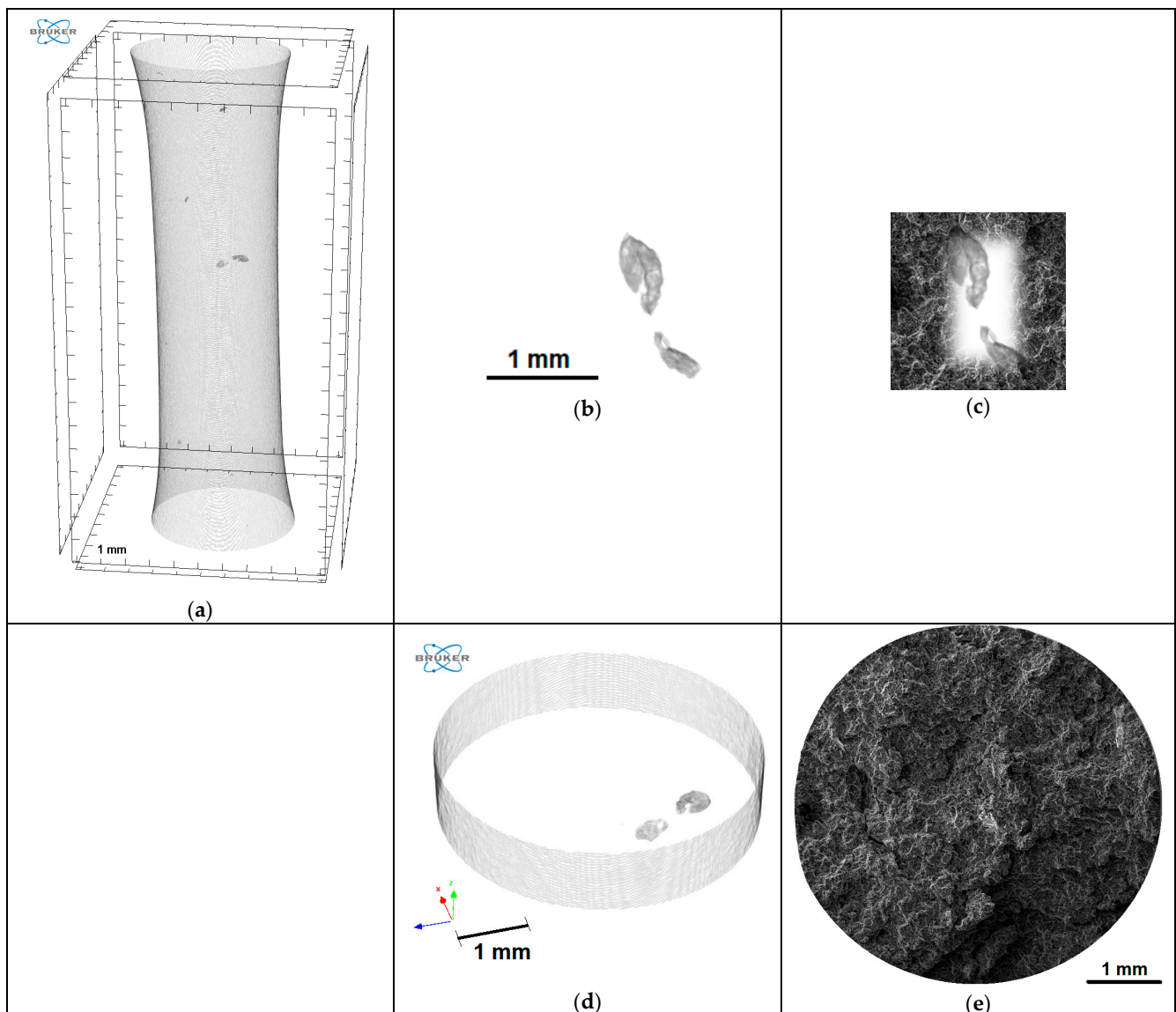


**Figure 9.** Gauge length of sample before loading (first  $R = -1$ ,  $2 \times 10^6$  cycles at 50 MPa run out followed by tensile test) in  $\mu$ -CT analysis (a,b,d) and fractured surface by SEM analysis (e) with highlighted large shrinkage cavity in (c).

The gauge length of a sample in Figure 10a reveals no defects of significant size while only a few small shrinkage cavities and pores are seen in the  $\mu$ -CT analysis. Figure 10b shows the network of second phases and only a few clusters can be seen. Unidirectional fatigue loading (compression load of  $-50$  MPa at  $R = -\infty$ ) was applied. It was of interest whether these pores and second phase clusters influence the failure position. The sample did not fail under fatigue loading up to  $2 \times 10^6$  cycles. The following parameters were measured by the final tensile test: TYS of 79 MPa, UTS of 129 MPa, and an elongation at fracture 0.61%. The hardness values after final fracture are mostly increased in the dendritic Mg-matrix (116%) and blocky Ba-rich phases (110%). The micrograph in Figure 10c shows horizontal micro cracks further away from the main crack, which did not open up significantly under the final tensile test, other than that seen in Figure 10d, where the secondary sub cracks closer to the main crack open by a great amount.



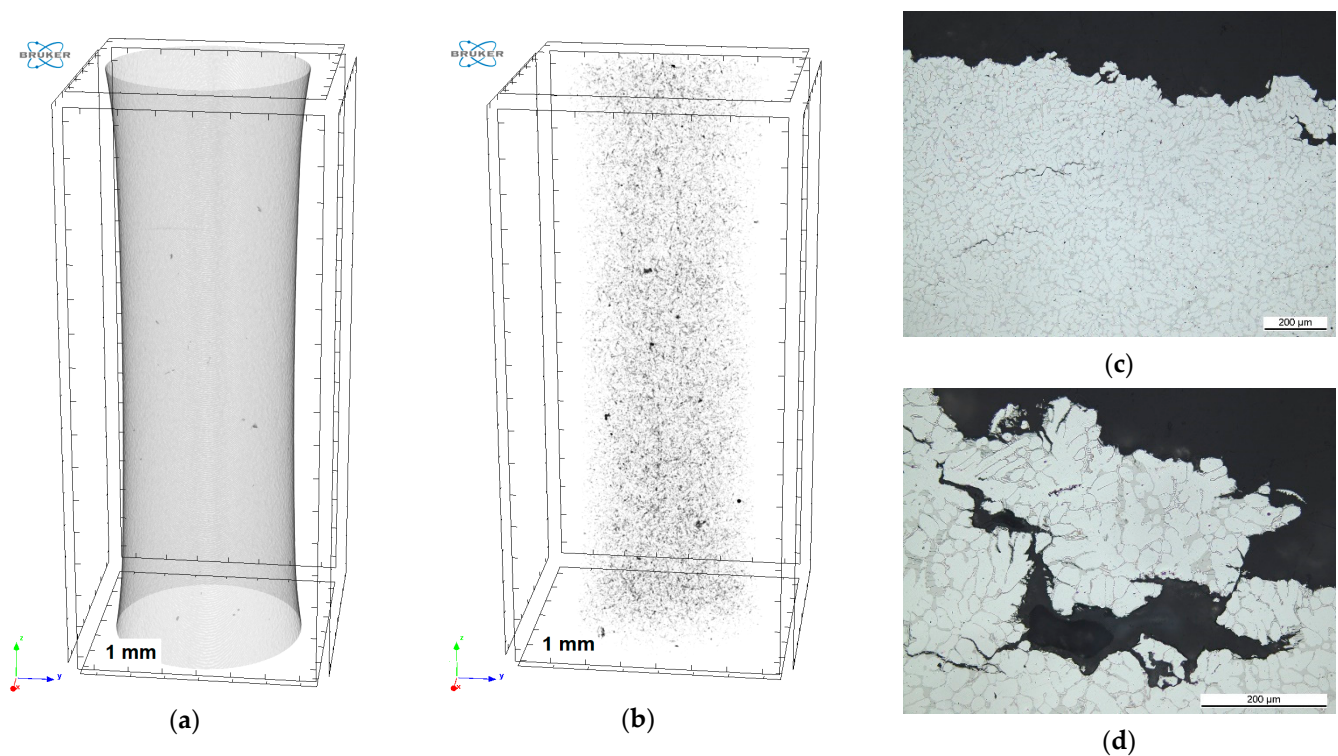


**Figure 10.** Gauge length of sample before loading (first  $R = -\infty$ ,  $2 \times 10^6$  cycles at  $-50$  MPa run out followed by tensile test) in  $\mu$ -CT analysis, pores in (a) and network of second phases in (b), cross-sectional micrographs of fracture surface (c,d).

#### 4. Discussion

The shrinkage cavities of a significant amount and the sizes lower the mechanical properties under tensile load and fatigue loading where tensile stress is involved. When the porosity [8] is at a low level of 1.48%, the tensile properties were found to be higher: TYS at  $202.6 \pm 0.7$  MPa, UTS at  $229.6 \pm 5.8$  MPa, and El. at  $1.6 \pm 0.5\%$ . The influence of large pores on the tensile properties were also seen in [13] where a TYS of  $78.1 \pm 0.6$  MPa was found. The mechanical properties under compression are less dependent on the porosity; in [8] the CYS was found to be  $117.6 \pm 15.1$  MPa, in [13] the CYS was  $128.0 \pm 4.9$  MPa and the UCS was  $286.8 \pm 2.9$  MPa. The compressive properties of this alloy are slightly higher, even with a CYS of  $135.00 \pm 9.17$  MPa, and the UCS with  $282.55 \pm 4.42$  MPa is in the range seen in [13]. Less increase of stress intensity around pores (defects), which is more significant under tension [24,25] and the ability to strain-harden the most under compression—see here the highest hardness values in Figure 11a and the highest hardness increase under compression in Figure 11b—makes this loading condition more bearable and independent of porosity.

According to Figure 11a the compact Ba-rich phase  $\text{Mg}_{21}\text{Al}_3\text{Ba}_2$  shows the highest initial hardness and remains at the highest value, which is almost twice as hard as the lamellar Ca-rich  $\text{Al}_2\text{Ca}$  region. The dendritic Mg-matrix has the lowest value, but hardens the most under compression, followed by the fully reversed fatigue testing method ( $R = -1$ ), where there is a significant part of the compression forces. By the increase in hardness, Figure 11b shows that the second phases do not change much under tensile and fatigue loading ( $R = 0$ ), but rather under compression and fully reversed fatigue,  $R = -1$ , where the monitoring of the hysteresis reveals compression creep with ongoing fatigue at stresses of 97% of TYS and 37% of CYS (50 MPa). The dendritic Mg-matrix strain-hardens significantly under compression, up to 152%. The twinned microstructure reveals a certain amount of plastic deformation. However, the low initial hardness remains at the lowest level in comparison to the second phases. The hardness increase of lamellar Ca-rich phase  $\text{Al}_2\text{Ca}$

is comparable with the dendritic Mg-matrix, and the Ba-rich phase  $\text{Mg}_{21}\text{Al}_3\text{Ba}_2$  is less pronounced under tensile and unidirectional fatigue testing,  $R = 0$ —this phase does not play a significant role under tensile deformation. With  $R = 0$  at 50 MPa the samples last 43,000 cycles at fracture and obviously show tensile creep, but the strain hardening is similar to the tensile quasi-static overload.

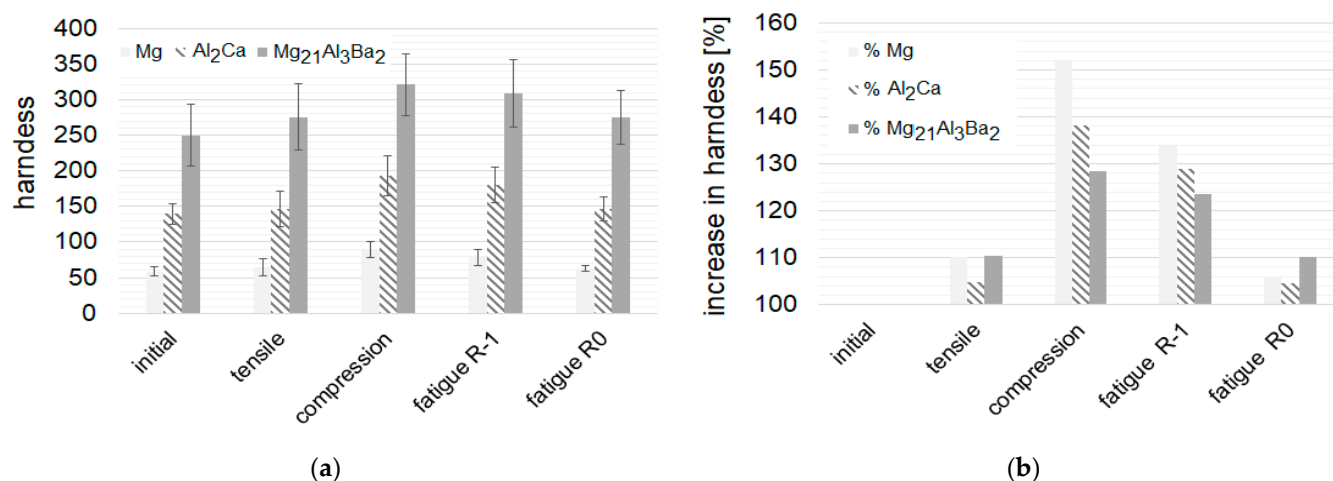


**Figure 11.** Bar charts of the hardness and hardness increase of the  $\alpha$ -Mg grains, the lamellar Ca-rich phase  $\text{Al}_2\text{Ca}$  and the blocky Ba-rich phase  $\text{Mg}_{21}\text{Al}_3\text{Ba}_2$  before and after loading, absolute values (a) and increase in percentage compared to the initial hardness (b).

By the cross-sectional micrographs of the fracture surfaces after tensile compression and fatigue load, it becomes clear that only fatigue loading causes transgranular cracking within the dendritic  $\alpha$ -Mg grains within the fatigue crack propagation region. In the region of residual fracture, the crack transforms into interdendritic cracking, where the hard and brittle second phases are located. In tensile and compression loading the crack initiates and propagates mainly through the compact Ba-rich phase  $\text{Mg}_{21}\text{Al}_3\text{Ba}_2$  via transgranular cracking, bridged by the lamellar Ca-rich phase  $\text{Al}_2\text{Ca}$ . Only when the shear deformation under compression is very high, just before final failure, does the crack appear to run through the  $\alpha$ -Mg dendrites. The second phases are more than twice ( $\text{Al}_2\text{Ca}$ ) and four times as hard ( $\text{Mg}_{21}\text{Al}_3\text{Ba}_2$ ) as the dendritic  $\alpha$ -Mg matrix, even after deformation; when the dendritic  $\alpha$ -Mg matrix hardens the most, the  $\text{Mg}_{21}\text{Al}_3\text{Ba}_2$  phase remains twice as hard as  $\text{Al}_2\text{Ca}$ . That means that in quasi-static loading the irreversible deformation is only concentrated on the hard and brittle phases, in agreement with the simple fracturing mode. Microstructural investigation in the study by [18] also confirmed that the crack growth mode changed from transdendritic to interdendritic. The transdendritic cracks occurred by a fatigue mechanism and the interdendritic cracks by overload. This study claims that this cracking mode transition phenomenon is one of the typical features of casting fracture by a fatigue mechanism.

Only during fatigue loading does the crack propagate into the softer dendritic  $\alpha$ -Mg matrix. The fully reversed loading mode causes increased stress intensity in the softer dendritic  $\alpha$ -Mg matrix near the interface to the brittle phases. Microcracks are the result of an accumulation of twins and slip bands in the softer dendritic  $\alpha$ -Mg matrix, which has a higher possibility to deform by having a quarter of the hardness of the  $\text{Mg}_{21}\text{Al}_3\text{Ba}_2$  phase. The fatigue crack initiation of Mg-alloys is also closely related to the deformation mechanisms of twinning [26]. Máthis et al. [27] interpreted their results on the investigation of tension–compression asymmetry in Mg by the dominant effect of twinning up to 200 °C and greater slip activity at higher temperatures. The dynamic crack propagation is therefore found in the form of three-dimensional fracturing with crack branching, see magnified image in Figure 12a from Figure 8. Figure 12b shows fine sub-crack branching into the softer dendritic  $\alpha$ -Mg matrix, where a redirection by the twinned microstructure can be seen.

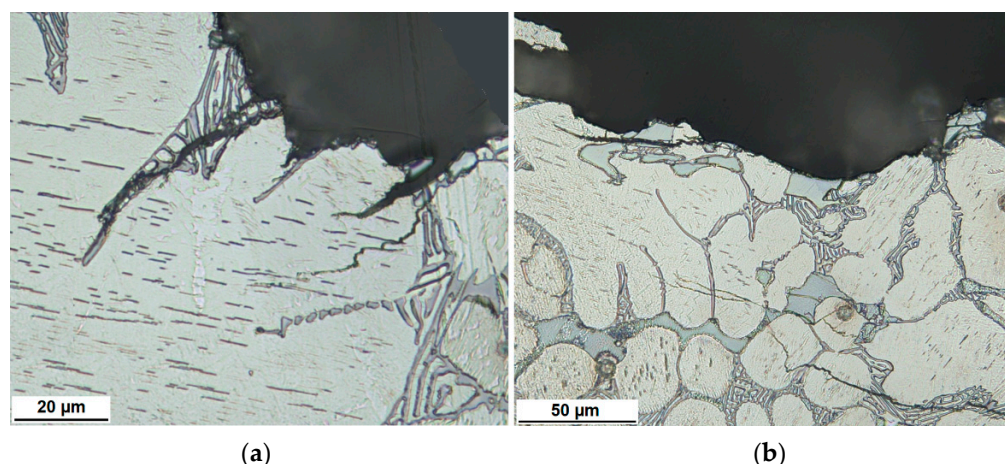


**Figure 12.** Cross-sectional micrographs of fracture surface after fatigue load ( $R = -1$ , 12,000 cycles) showing crack branching of the sub-cracks near the main crack, within the dendritic  $\alpha$ -Mg matrix (a,b).

The high hardness increase (Figure 11b) under compression can be explained by the delayed initiation and appearance of microcrack-compression loading being rather defect closing than crack opening [24,25]: even though [28] deformation modes are missing, all phases strain-harden the most under compression. The dendritic  $\alpha$ -Mg grain, which is the most deformable one among the three phases (lowest initial hardness), strain-hardens the highest, up to 152%. However, the compact Ba-rich phase  $\text{Mg}_{21}\text{Al}_3\text{Ba}_2$  stays at the highest hardness by a significant amount and is the phase which cracks first due to brittleness.

In addition to being interested in the change of the mean hardness value by the different loading modes, the hardness along the fractured surface is also of concern. The cross-sectional micrographs of fracture surfaces after fatigue load from Figure 6 ( $R = 0$ , 43,000 cycles) and Figure 8 ( $R = -1$ , 12,000 cycles) were used to evaluate the hardness at different regions. The hardness was measured within the fatigue crack propagation region near crack initiation, where transgranular cracking within the dendritic  $\alpha$ -Mg grains was seen in the middle of the fractured surface, where clearly only transgranular cracking within the brittle blocky Ba-rich phase  $\text{Mg}_{21}\text{Al}_3\text{Ba}_2$  and lamellar Ca-rich phase  $\text{Al}_2\text{Ca}$  occurs, and also within the residual fracture surface at the opposite side to the crack initiation region. It can be seen during unidirectional testing at 50 MPa ( $R = 0$ ) that up to 43,300 cycles to fracture the hardness of the blocky Ba-rich phase  $\text{Mg}_{21}\text{Al}_3\text{Ba}_2$  in the middle of the sample within the residual fracture region, is higher than within the fatigue crack propagation region, and is reduced at the final part of the residual fracture region, see Figure 13a. The lamellar Ca-rich phase  $\text{Al}_2\text{Ca}$  on the other hand increases slightly only at the final part of the residual fracture region. The softer dendritic  $\alpha$ -Mg grains increase slightly during fatigue loading with a slight decrease towards the final part of the residual fracture region. The fully reversed testing at 50 MPa ( $R = -1$ ) with the number of cycles to fracture of 12,000 shows a different picture, see Figure 13b. Here the highest hardness values were found in the region of the fatigue crack propagation, the blocky Ba-rich phase  $\text{Mg}_{21}\text{Al}_3\text{Ba}_2$  strain-hardens the most, followed by the softer dendritic  $\alpha$ -Mg grains. The increased hardness compared to the undeformed material (initial) remains in the residual fracture region for the blocky Ba-rich phase  $\text{Mg}_{21}\text{Al}_3\text{Ba}_2$ , which strain-hardens the most, followed by the softer dendritic  $\alpha$ -Mg grains.



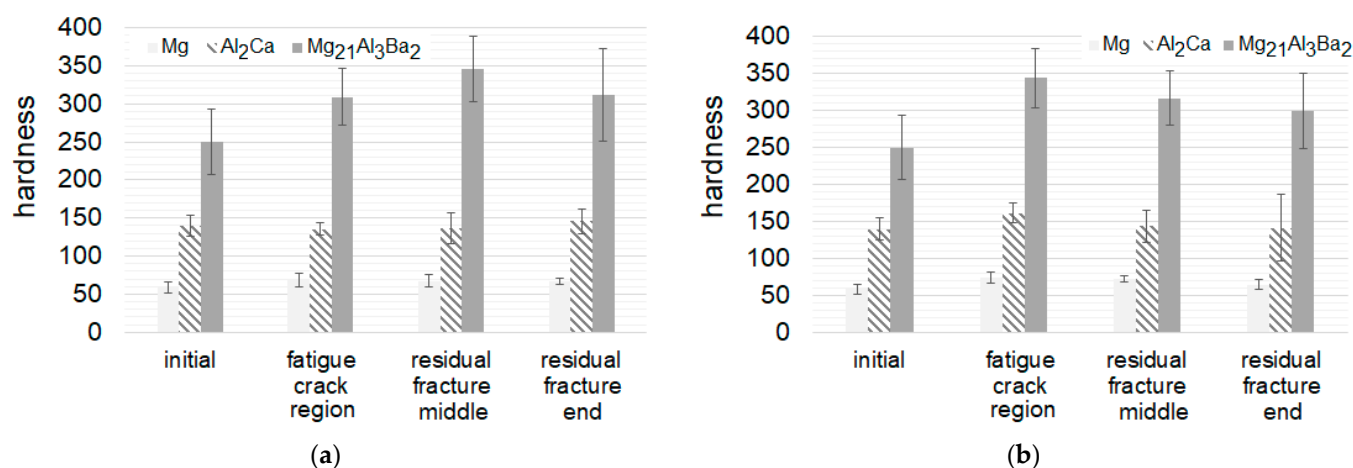


**Figure 13.** Bar charts of the hardness of the  $\alpha$ -Mg grains, the lamellar Ca-rich phase  $\text{Al}_2\text{Ca}$  and the blocky Ba-rich phase  $\text{Mg}_{21}\text{Al}_3\text{Ba}_2$  before and after fatigue loading in different regions of the crack propagation, at  $R = 0$  with 43,300 cycles at fracture, taken from micrograph in Figure 6 (a) and at  $R = -1$  with 12,000 cycles at fracture, taken from micrograph in Figure 8 (b).

These results show that the three phases in the DieMag633 not only strain-harden in a different amount depending on the loading conditions, tensile, compression, and fatigue, but also depend on the fatigue testing method and the specific region of crack propagation. Whereas in fully reversed loading ( $R = -1$ ), where compression stress at a level of 37% of the CYS on top of the tensile stress at a level of 97% of the TYS is applied (reversed loading in compression seems to benefit, one sample lasted up to 2,000,000 cycles run out), the blocky Ba-rich phase  $\text{Mg}_{21}\text{Al}_3\text{Ba}_2$  strain-hardens the most during fatigue crack propagation (together with the lamellar  $\text{Al}_2\text{Ca}$  phase). This phase hardens less in this region under unidirectional loading, but more in the region where the crack propagation has changed into interdendritic and transgranular cracking within the hard second phases.

To measure the hardness along the fractured surface in shorter distances is the focus of the current work and will be published together with more statistically validated data from further fatigue testing.

The micrographs as well as the images from the  $\mu$ -CT analysis reveal many sub-cracks branching from the main crack along or rather within the interdendritic brittle phases (plus transgranular within the  $\alpha$ -Mg matrix during fatigue loading), which reach up to 100  $\mu\text{m}$  into the material. These cracks often interconnect with pores and cavities. The microstructure is highly twinned along the main crack and around the sub-cracks, see Figure 14a,b. Since twinning is a dominant deformation mode in Mg-alloys [29], the hardness increase can be explained by the visible change of the microstructure, see Figure 14b. However, the microstructure in the fractured surfaces after tensile loading is highly twinned, but with a lower increase in hardness. It is noticeable that the cross-sectional micrographs of the fracture surfaces after tensile loading show a lot of large sub-cracks, and often further surface cracks, see Figure 14a. It can be assumed, that the absorbed energy caused the microcracks in the brittle second phases rather than deforming the phases. The ability to play a part in the deformation under tension is low in all three phases, see smaller hardness increase for tensile and fatigue  $R = 0$  testing in Figure 11b. Even so, the softer dendritic  $\alpha$ -Mg matrix still twins before final fracture but the onset twinning is rather low [30].

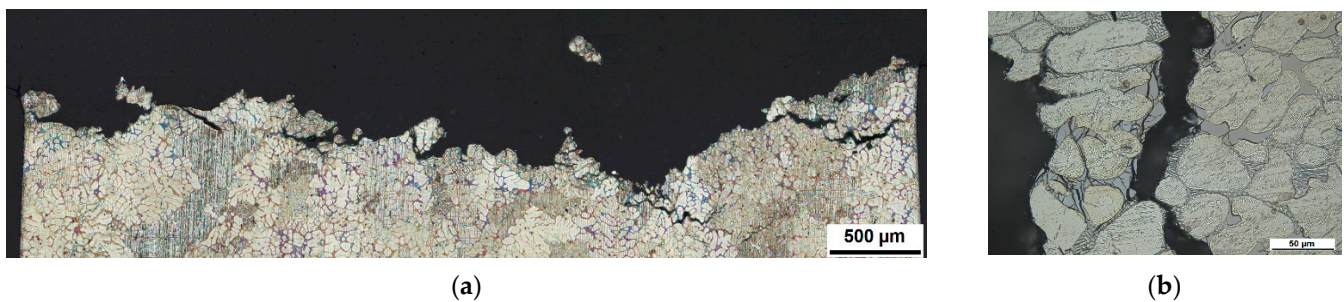


**Figure 14.** Cross-sectional micrographs of fracture surface after tensile load showing many sub-cracks branching off the main crack (a) and magnified area showing highly twinned microstructure (b).

The samples failed by fatigue testing showed less large sub-cracks (compare Figures 6 and 8 to Figure 14). They are mainly located at the crack propagation region or the transition region to the residual cracking, and they also give a good indication of the direction of the fatigue crack propagation. The cracks are influenced by the pores and shrinkage cavities, which often accompany the crack growth. When unidirectional loading is applied the hardness value increases are similar to tensile loading. This can be explained by the fact that at the “ $R = 0$ ” sequences, only (positive) tensile stresses are applied.

In the region where under fatigue loading most of the larger sub-cracks were found, transgranular cracking within the softer dendritic  $\alpha$ -Mg matrix was seen, which hardens the most within this fatigue crack propagation region—up to 117% for  $R = 0$  and very significant (together with the other phases) up to 126% for  $R = -1$ . Only the compression load causes higher strain hardening with 152%.

First  $\mu$ -CT analysis reveals that large shrinkage cavities, which are also near the area of the lowest diameter in the gauge length, influence the location of the fracture surface. When large shrinkage cavities are away from the lowest diameter region, they do not influence the fracture under fatigue loading, but rather under tensile loading.

During fully reversed fatigue testing, compression creep was seen accompanied with strain-hardening. The high hardness increase within the brittle second phases, but also in the dendritic  $\alpha$ -Mg matrix, can be attributed to the compression part of the reversed loading sequences. This strain-hardening becomes very clear from the tensile test data after  $2 \times 10^6$  cycles to run out: TYS increases by a factor of 1.9 (98 MPa) and the UTS by a factor of 1.3 (132 MPa), whereas the elongation at fracture was reduced to 74% (0.43%). The hardness increase after the final fracture from the tensile test shows hardness values in which the strain-hardening amount contains parts from fatigue loading strengthening and hardening from the tensile test.

The sample exposed to unidirectional fatigue loading ( $R = -\infty$  at  $-50$  MPa) was free of large pores and shrinkage cavities. The strain-hardening amount which was obtained from the final tensile test after the “ $2 \times 10^6$  cycles run out” is smaller than that seen after fully reversed fatigue testing. The TYS increased by 1.53 to 79 MPa, the UTS by 1.26 to 129 MPa, and an elongation at fracture stayed with 0.61% with the range of initially measured values. Even compression loading showed a great effect on the hardness change on all phases, the hardness increase of the fractured surface of the unidirectional fatigue loaded sample was also found to be smaller compared to fully reversed fatigue testing. This can be explained by the stress amount applied: 50 MPa is far less than the CYS (37%), but very close to the TYS (97%). The reduction of elongation at fracture, seen in the tensile test after fully reversed fatigue testing, is a result of the significant increase in yield strength of almost 200%, but also with a large shrinkage cavity. The micrographs of the unidirectional fatigue exposed sample at  $-50$  MPa after tensile testing revealed thinner, horizontal micro-cracks away from the main crack, which might have formed during compression fatigue loading within the brittle second phases but did not open up in a significant amount under the final tensile test. A high amount of larger secondary sub cracks will most certainly have their origin in these thinner cracks. Further, a statistically validated number of tests will show

whether this fracture procedure is a characteristic of unidirectional fatigue loading under compression and if less strain-hardening is a result of this. In general, the hardness increase is found to be higher in samples which failed during the fatigue test compared to the “run out” samples, and since the damage was pre-fatigue crack propagation the crack follows the interdendritic network of second phases instead of propagation through the Mg-matrix. Transgranular crack propagation within the Mg-matrix has only been seen under fatigue crack growth.

## 5. Conclusions

This study showed the strong influence of brittle interdendritic second phases on crack propagation under load in a cast Mg-Al-Ba-Ca (DieMg633) alloy. The material consisted of primary  $\alpha$ -Mg dendrites and two interdendritic phases, the lamellar  $\text{Al}_2\text{Ca}$  and the blocky  $\text{Mg}_{21}\text{Al}_3\text{Ba}_2$ . The highest hardness was seen in  $\text{Mg}_{21}\text{Al}_3\text{Ba}_2$ , followed by  $\text{Al}_2\text{Ca}$ . The material was exposed to different loading conditions and the phases played a different role depending on tensile, compression or fatigue loading. Most of the crack propagation was transgranular within the hard and brittle phases (interdendritic), the lamellar  $\text{Al}_2\text{Ca}$  phase mainly bridges the cracks from the even harder blocky  $\text{Mg}_{21}\text{Al}_3\text{Ba}_2$  phases, in which the microcracks initiate. Transgranular crack propagation within the Mg-matrix was only found in fatigue loading within the crack propagation region.

The material behaved as very brittle under tension; here, the hardness increase of the phases during deformation was rather low and no plastic deformation was seen. The material in the present study contained inhomogeneously distributed pores and shrinkage cavities of large size, which also reduce the tensile properties. Different loading conditions showed different degrees of strain hardening within the three phases. At  $R = 0$ , for example, the hardness increase of the phases was found to be the highest within the crack propagation region.

The micrographs revealed a stronger influence of crack propagation of the hard and brittle phase rather than the smaller pores and shrinkage cavities; large shrinkage cavities obviously cause an increase of stress intensity and locate the crack along these defects.

The role of the phases on the change of mechanical properties during deformation and crack propagation under different load conditions will help to understand fracture mechanics in Mg-Al-Ba-Ca alloys and will provide information about preferred load conditions and their limitations, and thus the selected application sites. The material performed the best under compression loading, where the porosity and brittleness were less effective.

**Author Contributions:** Conceptualization, P.M.; methodology, P.M.; validation, all; formal analysis and investigation, D.G. and B.C.; resources, N.H.; data curation, B.C.; writing—original draft preparation, P.M.; writing—review and editing, all; visualization, D.G. and B.C.; supervision, N.H. All authors have read and agreed to the published version of the manuscript.

**Funding:** This research received no external funding.

**Institutional Review Board Statement:** Not applicable.

**Informed Consent Statement:** Not applicable.

**Data Availability Statement:** Not applicable.

**Conflicts of Interest:** The authors declare no conflict of interest.

## References

1. Powell, B.R.; Rezhets, V.; Balogh, M.P.; Waldo, R.A. Microstructure and creep behavior in AE42 magnesium die-casting alloy. *JOM* **2002**, *54*, 34–38. [[CrossRef](#)]
2. Luo, A.A. Recent magnesium alloy development for elevated temperature applications. *Int. Mater. Rev.* **2004**, *49*, 13–30. [[CrossRef](#)]
3. Suzuki, A.; Saddock, N.D.; Jones, J.W.; Pollock, T.M. Structure and transition of eutectic (Mg,Al)<sub>2</sub>Ca Laves phase in a die cast Mg–Al–Ca base alloy. *Scr. Mater.* **2004**, *51*, 1005–1010. [[CrossRef](#)]

4. Luo, A.A.; Powell, B.R.; Sachdev, A.K. Computational phase equilibria and experimental investigation of magnesium-aluminum-calcium alloys. *Intermetallics* **2012**, *24*, 22–29. [[CrossRef](#)]
5. Buha, J. The effect of Ba on the microstructure and age hardening of an Mg–Zn alloy. *Mater. Sci. Eng. A* **2008**, *491*, 70–79. [[CrossRef](#)]
6. Dieringa, H.; Huang, Y.; Wittke, P.; Klein, M.; Walther, F.; Dikovits, M.; Poletti, C. Compression-creep response of magnesium alloy DieMag422 containing barium compared with the commercial creep-resistant alloys AE42 and MRI230D. *Mater. Sci. Eng. A* **2013**, *585*, 430–438. [[CrossRef](#)]
7. Dieringa, H.; Zander, D.; Gibson, M.A. Creep Behaviour Under Compressive Stresses of Calcium and Barium Containing Mg–Al-based Die Casting Alloys. *Mater. Sci. Forum* **2013**, *765*, 69–73. [[CrossRef](#)]
8. Gavras, S.; Zhu, S.; Easton, M.A.; Gibson, M.A.; Dieringa, H. Compressive Creep Behavior of High-Pressure Die-Cast Al-Containing Magnesium Alloys Developed for Elevated Temperature Applications. *Front. Mater.* **2019**, *6*, 262. [[CrossRef](#)]
9. Wittke, P.; Klein, M.; Walther, F. Chemical–mechanical characterization of the creep-resistant Mg–Al–Ca alloy DieMag422 containing barium. *Mater. Test.* **2014**, *56*, 16–23. [[CrossRef](#)]
10. Walther, F. Microstructure-Oriented Fatigue Assessment of Construction Materials and Joints Using Short-Time Load Increase Procedure. *Mater. Test.* **2014**, *56*, 519–527. [[CrossRef](#)]
11. Wittke, P.; Klein, M.; Dieringa, H.; Walther, F. Corrosion fatigue assessment of creep-resistant magnesium alloy Mg–4Al–2Ba–2Ca in aqueous sodium chloride solution. *Int. J. Fatigue* **2016**, *83*, 59–65. [[CrossRef](#)]
12. Klein, M.; Walther, F. Electrochemical-controlled Characterization of the Corrosion Fatigue Behavior of Creep-resistant Magnesium Alloys DieMag422 and AE42. *Procedia Eng.* **2016**, *160*, 158–166. [[CrossRef](#)]
13. Teschke, M.; Koch, A.; Walther, F. Comparison of High-Temperature Compression and Compression–Compression Fatigue Behavior of Magnesium Alloys DieMag422 and AE42. *Materials* **2020**, *13*, 497. [[CrossRef](#)] [[PubMed](#)]
14. Jain, J.; Poole, W.J.; Sinclair, C.W.; Gharghouri, M.A. Reducing the tension–compression yield asymmetry in a Mg–8Al–0.5Zn alloy via precipitation. *Scr. Mater.* **2010**, *62*, 301–304. [[CrossRef](#)]
15. Lv, C.; Liu, T.; Liu, D.; Jiang, S.; Zeng, W. Effect of heat treatment on tension–compression yield asymmetry of AZ80 magnesium alloy. *Mater. Des.* **2012**, *33*, 529–533. [[CrossRef](#)]
16. Park, S.H.; Lee, J.H.; Moon, B.G.; You, B.S. Tension–compression yield asymmetry in as-cast magnesium alloy. *J. Alloys Compd.* **2014**, *617*, 277–280. [[CrossRef](#)]
17. Li, Z.; Luo, A.A.; Wang, Q.; Zou, H.; Dai, J.; Peng, L. Fatigue characteristics of sand-cast AZ91D magnesium alloy. *J. Magnes. Alloys* **2017**, *5*, 1–12. [[CrossRef](#)]
18. Park, M.; Hwang, Y.-H.; Choi, Y.-S.; Kim, T.-G. Analysis of a J69-T-25 engine turbine blade fracture. *Eng. Fail. Anal.* **2002**, *9*, 593–601. [[CrossRef](#)]
19. Park, S.; Kayani, S.H.; Kim, H.; Jung, I.D.; Reddy, N.S.; Euh, K.; Seol, J.B.; Kim, J.G.; Sung, H. Effect of Interdendritic Precipitations on the Mechanical Properties of GBF or EMS Processed Al–Zn–Mg–Cu Alloys. *Crystals* **2021**, *11*, 1162. [[CrossRef](#)]
20. Ma, Z.; Samuel, A.M.; Doty, H.W.; Samuel, F.H. On the Fractography of Impact-Tested Samples of Al–Si Alloys for Automotive Alloys. In *Fracture Mechanics–Properties, Patterns and Behaviours*; Alves, L., Ed.; IntechOpen: London, UK, 2016; ISBN 978-953-51-2709-3. [[CrossRef](#)]
21. Merlin, M.; Timelli, G.; Bonollo, F.; Garagnani, G.L. Impact behaviour of A356 alloy for low-pressure die casting automotive wheels. *J. Mater. Process. Technol.* **2009**, *209*, 1060–1073. [[CrossRef](#)]
22. Zýka, J.; Málek, J.; Hrbáček, K. Mechanical properties and microstructure of large IN713LC nickel superalloy castings. *MATEC Web Conf.* **2014**, *14*, 21004. [[CrossRef](#)]
23. Monobe, L.S.; Schön, C.G. Microstructural and fractographic investigation of a centrifugally cast 20Cr32Ni+Nb alloy tube in the ‘as cast’ and aged states. *J. Mater. Res. Technol.* **2013**, *2*, 195–201. [[CrossRef](#)]
24. Wolf, E. Fatigue crack closure under cyclic tension. *Eng. Fract. Mech.* **1970**, *2*, 37–45. [[CrossRef](#)]
25. Pippan, R.; Hohenwarter, A. Fatigue crack closure: A review of the physical phenomena. *FFEMS Fatigue Fract. Eng. Mater. Struct.* **2017**, *40*, 471–495. [[CrossRef](#)] [[PubMed](#)]
26. Wang, B.J.; Xu, D.K.; Wang, S.D.; Han, E.H. Fatigue crack initiation of magnesium alloys under elastic stress amplitudes: A review. *Front. Mech. Eng.* **2019**, *14*, 113–127. [[CrossRef](#)]
27. Máthis, K.; Čapek, J.; Zdražilová, Z.; Trojanová, Z. Investigation of tension–compression asymmetry of magnesium by use of the acoustic emission technique. *Mater. Sci. Eng. A* **2011**, *528*, 5904–5907. [[CrossRef](#)]
28. Reed-Hill, R.E.; Robertson, W.D. Additional modes of deformation twinning in magnesium. *Acta Metall.* **1957**, *5*, 717–727. [[CrossRef](#)]
29. Barnett, M.R. Twinning and the ductility of magnesium alloys: Part II. “Contraction” twins. *Mater. Sci. Eng. A* **2007**, *464*, 8–16. [[CrossRef](#)]
30. Kumar, M.A.; Clausen, B.; Capolungo, L.; McCabe, R.J.; Liu, W.; Tischler, J.Z.; Tomé, C.N. Deformation twinning and grain partitioning in a hexagonal close-packed magnesium alloy. *Nat. Commun.* **2018**, *9*, 4761. [[CrossRef](#)]